Climate Dynamics (2024) 62:955–972
https://doi.org/10.1007/s00382-023-06959-5

ORIGINAL ARTICLE

Emphasizing the land use-cloud-radiation feedback in detecting climate effects of land use and land cover changes

Deming Zhao[1] · **Jinlin Zha**[1,2] · **Jian Wu**[2]

Received: 21 May 2023 / Accepted: 8 September 2023 / Published online: 16 September 2023

Abstract
Previous assessments on climate effects of land use and land cover changes (LUCC) mostly focused on the altered surface upward shortwave radiation flux due to changes in surface albedo. However, the explorer on the physical mechanism using the Weather Research and Forecasting model with subgrid scale process precisely described here revealed that the LUCC impacts could not be directly interpreted by surface albedo changes only. The land use-cloud-radiation feedback, within which cloud amount and cloud ceiling, large-scale circulation related moisture flux and local evaporation were altered, played an essential role in affecting surface energy and water budgets between land surface and the atmosphere, especially for the impacted downward shortwave radiation flux. With subgrid scale process considered in describing LUCC and the land use-cloud-radiation feedback emphasized, LUCC impacts on surface air temperature (SAT), precipitation and near-surface wind speed (NSWS) were explored, which displayed marked temporal and spatial characteristics. The LUCC climate effects for both the influenced terrestrial subregions and the intensity were larger over summertime, expressing marked affection on the East Asian Summer Monsoon system. The LUCC impacts on SAT and NSWS mainly presented as changes in mean state, whereas the influences on the precipitation principally displayed as changes in the variability. LUCC induced changes in the averaged SAT, precipitation and NSWS were small, whereas the nearly symmetric distributions between positive and negative changes, which contributed to total changes, were much larger and might have a considerable impact on local and regional climate, especially on extreme climate events.

Keywords Land use and land cover changes · The land use-cloud-radiation feedback · Subgrid scale process · Mean climate state · The variability

1 Introduction

Land use and cover change (LUCC) can have influences on local, regional, and even global climate and environment through biogeophysical and biogeochemical processes. The biogeochemical affections reflect LUCC impacted changes in emissions or removals of carbon dioxide (CO2), methane (CH4) and nitrous oxide (N_2O), as well as emissions of precursors of short biogenic volatile organic compounds (BVOC) and aerosols (Defries et al. 1999; Houghton and Nassikas 2017; Nisbet et al. 2019; Gasser et al. 2020). Many studies have been performed to explore LUCC biogeochemical effects, whereas much more works have concentrated on LUCC biogeophysical effects. The biogeophysical effects include changes in surface albedo, roughness length, evapotranspiration, etc., with which the interactions of momentum, energy, and water between land surface and atmosphere are altered (Charney 1975; Betts et al. 2007; Alkama and Cescatti 2016; Hirsch et al. 2018; Boyaj et al. 2020; Li et al. 2023). Meanwhile, studies on the combined biogeophysical and biogeochemical effects have also been conducted (Bathiany et al. 2010; Pongratz et al. 2010; Lawrence et al. 2012; Ward et al. 2014; Liu et al. 2022). On global scale, the warming from LUCC biogeochemical effects (due to changes in land greenhouse gas emissions or removal) is partly damped by the cooling from the corresponding biogeophysical effects due to changes in surface albedo (Jia et al. 2019). LUCC induced changes in surface albedo were assumed to induce a negative radiative

[1] CAS Key Laboratory of Regional Climate and Environment for Temperate East Asia, Institute of Atmospheric Physics, Chinese Academy of Sciences, Beijing 100029, China

[2] Key Laboratory of Atmospheric Environment and Department of Atmospheric Science, Yunnan University, Kunming 650091, China

forcing of -0.20 ± 0.10 W m^{-2} (medium confidence) from the Sixth Assesment Report (AR6), showing the varied values of -0.15 ± 0.10 W m^{-2} from the fifth Assesment Report (AR5) and -0.20 ± 0.20 W m^{-2} from the fourth Assesment Report (AR4), which reveals that the evaluations on LUCC impacts still have much uncertainty (IPCC 2007; 2013; 2021). However, on regional or local scales, LUCC can be of high heterogeneity and displays significant subregional characteristics due to intense human activities, which results in quite different affections on the climate with much more uncertainties, compared to those at global scale (Zhou et al. 2019).

Observation minus reanalysis method has been widely used to evaluate LUCC impacts, assuming that land surface information is rarely included in the assimilation and fitting process of the reanalysis data (Kalnay and Cai 2003), especially adopted to quantitatively evaluate the urbanization's warming effects. However, the scarcity of the observational data and high spatial heterogeneity of the meteorological observation stations, as well as the coarse resolution of the reanalysis data make this method be of much limitation. Meanwhile, the method using urban meteorological observation minus rural meteorological observation has also been adopted to detect the urbanization effects (Gallo et al. 1999). However, due to the difficulties in identifying the 'real' rural stations, as well as the spatial heterogeneity of the meteorological observation stations and the inhomogeneization of the observational data, much uncertainty exists from this approach (Yan et al. 2010).

In order to explore LUCC impacts on historical climate and future climate projection, numerical simulations have been widely adopted using different models, including land surface models (LSMs), regional climate models (RCMs) and general circulation models (GCMs). LSMs includes the Noah land surface model (Noah, Chen et al. 2007), the Community Land Model (CLM, Oleson et al. 2010), the community Noah land surface model with multi-parameterization options (Noah-MP, Niu et al. 2011), etc. RCMs include the Weather Research and Forecasting Model (Skamarock et al. 2008), the Regional Climate Model system (RegCM4, Giorgi et al. 2012), the Regional Integrated Environment Modeling System (RIEMS, Wang et al. 2015), etc. GCMs include the Community Earth System Model (CESM, Vertenstein et al. 2012), the Max Planck Institute Earth System Model (MPI-ESM, Mueller et al. 2018), etc. With the recognition of LUCC affections on the climate at different spatiotemporal scales, especially at local and regional scales, high-resolution RCMs, which can reflect fine topographical and land surface information, and describe detailed land use information and the corresponding changes, are regarded as a good approach to explore LUCC impacts on energy and water cycle and regional climate (Gao et al. 2006; Rasmussen et al. 2014; Shi et al. 2017; Zhao and Wu 2017a). Though large numbers of projects and studies have been performed to explore LUCC impacts on the climate, much uncertainty still exists, especially at regional scales. The uncertainty might result from the scarcity of the observational data, various land use dataset from different resources (Chinnisamy et al. 2008) or in different spatial scale (Huang et al. 2007), different RCMs with varied LSMs and different parameterization schemes (cumulus parameterization options, radiation physics options, microphysics options, and planetry boundary layer options, etc.) from RCMs employed in the LUCC impact studies, insufficient understanding of the physical mechanism for the LUCC impacts, etc.

The exchanges of energy and water between land surface and the atmosphere have been proven to play an important role for climate changes at different spatial scales, especially at local and regional scales (Zhang et al. 2018). Meanwhile, LUCC might be less at a certain model grid with coarse resolution, while more pronounced with subgrid scale process considered. Therefore, in order to explore LUCC impacts on local and regional energy and water budget, it is necessary to make land use distributions and the corresponding changes be clearly represented by the mode grid cell. Numerical experiments with the mosaic approach adopted in the Noah LSM (Noah-mosaic) from the WRF model have been proven to precisely describe subgrid scale process of the LUCC and disclose the LUCC impacts (Li et al. 2013; Zhao and Wu 2017b).

LUCC can have significant impacts on people's daily production and life by affecting surface air temperature (SAT), the precipitation and near-surface wind speed (NSWS) for the influenced intensity, frequency and subregion area. Many previous studies have been performed on the LUCC impacts, which mostly regarded that the dominant LUCC biophysical effect is surface albedo and concentrated on LUCC induced changes in surface albedo, showing a cooling effect on global scale (Charney 1975; Betts 2000; Andrews et al. 2017; Jia et al. 2019). However, LUCC can also affect water cycle through altering streamflow and evapotranspiration (Jehanzaib et al. 2020). The impacts of LUCC induced water vapor change on the greenhouse contribution are negligible because of its short lifetime (Sherwood et al. 2018), whereas the radiative forcing can be altered through changing in cloud amount (IPCC 2021), for which fewer studies have been performed and much uncertainty exists, and the conclusions aren't precisely described in AR6 (IPCC 2021). Meanwhile, the LUCC affections on regional climate depend on the location and season, which expresses high spatial heterogeneity and seasonality (Jia et al. 2019).

Many conducted studies have revealed that LUCC induced changes in SAT expressed marked interannual variations, showing that LUCC induced SAT changes from

individual year might be quite different from those of long-term mean for both change intensity and positive/negative changes (see Supplementary Fig. S1), based on which the LUCC impacts might be overestimated or underestimated and the physical mechanism in interpreting LUCC influences might be inconsistent with the reality. Therefore, LUCC induced changes in energy and water budget and the impacts on East Asian monsoon system (EAM) for the years of 2006–2007, especially in summer (June, July and August, JJA), are selected and explored here in detail.

Spatial distributions for changes in SAT, precipitation, and NSWS at annual, seasonal and monthly scales in 2006–2007 using land use images from the 1980s (LU80) to 2010s (LU10) are firstly displayed. LUCC impacted terrestrial subregion area passing significance tests and changes in the averaged for SAT, precipitation and NSWS are then quantitatively evaluated. PDF distributions of LUCC impacted terrestrial subregion area for the averaged and PDF distributions of the influenced terrestrial subregion area for the changes of SAT, precipitation and NSWS at different grades are further analyzed. Finally, the exploring on physical mechanisms in interpreting the land use-cloud-radiation feedback is presented.

2 Numerical experimental design and data

2.1 Numerical experimental design

Numerical experiment desgon similar to the previous works (Zhao and Wu 2017b, c) are performed to emphasize the land use-cloud-radiation feedback in detecting climate effects of LUCC using the WRF model with Noah-mosaic approach. In order to make numerical experiments be clearly understandable, experiment design schemes are simply repeated here.

The simulated domain covers majority areas of East Asia with 288 and 228 model grids in the longitudinal and latitudinal directions, respectively, for which the topographical distribution is shown in Fig. S2 in the Supplementary. The central longitude and latitude of the simulated domain are 108.5°E and 35°N, respectively and the horizontal resolution is 30 km. There are 51 levels in the vertical direction with air pressure 10 hPa at the top of the model. The numerical experiments run from July 1, 2005 to March 01, 2007, for which the period from July 1, 2005 to February 28, 2006 is regarded as 'spin-up' time. Therefore, only the results for the period from March 1, 2006 to February 28, 2007 are analyzed, showing continuous four seasons: Spring (MAM: March-April-May, 2006); Summer (JJA: June-July-August, 2006); Autumn (SON: September-October-November, 2006); and Winter (DJF: December, 2006-January, 2007-February, 2007).

During the numerical experiments, eight dominant land use categories (Noah-mosaic approach) instead of only one dominant land use category (Noah LSM) in a certain model grid cell were adopted, based on which the computed surface parameters such as surface albedo, surface roughness length, etc. were more close to the real values. Therefore, land use distributions and LUCC, as well as land and atmosphere interactions can be well expressed with the Noah-mosaic approach (Li et al. 2013). Other physical parameterization schemes include the WSM 5-class scheme microphysics scheme, the RRTMG short-wave and long-wave radiation schemes, Mellor-Yamada-Janjic TKE boundary-layer scheme, and the Modified Tiedtke cumulus scheme (Skamarock et al. 2008). Meanwhile, the WRF model with modifications to the codes designed to fulfill some climate community requirements (CLWRF, Fita et al. 2010) was adopted, with which CO2 and other greenhouse gas concentrations such as N2O, CH4, CFC11 and CFC12 were read from the pre-generated file in the WRF model and could be correctly represented during the simulation periods for the years 2006 and 2007.

2.2 The observational data

The observational SAT data from University of East Anglia Climatic Research Unit (CRU, Harris et al. 2020) with a spatial resolution of 0.5° longitude and 0.5° latitude over land domains were adopted to test the performance of the WRF model in simulating SAT. The observational precipitation data Global Precipitation Analysis Products from Global Precipitation Climatology Center (GPCC, Schneider et al. 2020) with a spatial resolution of 0.5° longitude and 0.5° latitude over the land were used to make comparisons with the simulated results. The observational SAT and precipitation data were remapped to model grid cells with a spatial resolution of 30 km.

2.3 The driven data of the WRF

The driven data including initial conditions and time-varying boundary conditions updated every 6 h were provided by the National Centers for Environmental Prediction's (NCEP) FNL operational model global troposphere analyses with a spatial resolution 1.0° (available online at https://rda.ucar.edu/datasets/ds083.2/. https://doi.org/10.5065/D6M043C6).

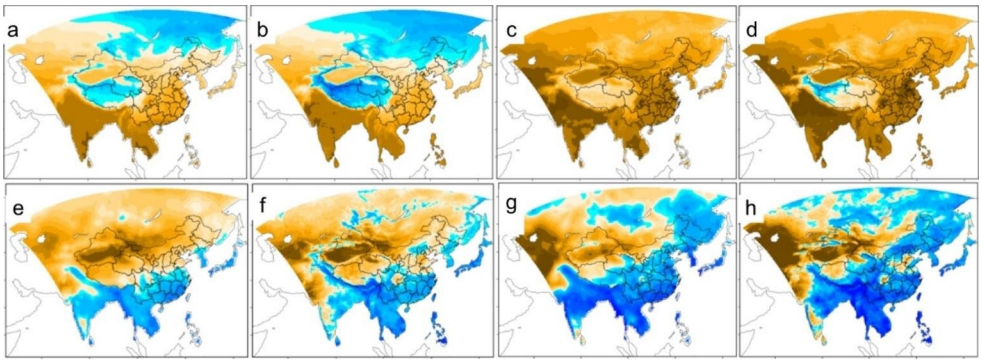

Fig. 1 Spatial distributions of the (**a**, **c**: CRU; **e**, **g**: GPCC) observational and (**b, d, f, h**) simulated (**a-d**, units: °C) SAT and (**e-h**: units: mm day^{-1}) precipitation with the default land use data in the model for (**a, b, e, f**) annual and (**c, d, g, h**) summer results

2.4 Land use data in the 1980 and 2010 s

Land use data in the 1980s (LU80) and 2010s (LU10) adopted in the numerical experiments are the same as those applied in Zhao and Wu (2017b, c). Detailed information on how land use data were retrieved based on satellite images were expressed by Li et al. (2017) and Yang et al. (2017), shown in the Supplementary Text S1. Descriptions on land use fraction changes from LU80 to LU10 are presented in Supplementary Fig. S3 and Text S2.

3 Results

3.1 Model's performance in simulating surface air temperature and precipitation

The simulated results using the WRF model with the default land use data in the model, and LU80 and LU10 were compared to the observational data for annual and summer mean SAT from CRU and the precipitation from GPCC, respectively (Fig. 1 and Fig. S4 in the Supplementary). In general, SAT and precipitation could be well reproduced by the model for both annual and JJA results, though bias existed.

The observational annual and JJA mean SAT could be well simulated, showing little differences for the spatial distribution and intensity (Fig. 1a and d and Figs. S4a-S4d). However, bias existed between the simulated and the observed. For annual results, SAT was underestimated, especially over the northern part of the simulated domain and the Tibet Plateau. For JJA values, SAT was little overestimated, especially in the southern part of the simulated domain.

The observational precipitation, showing larger in the southern part and smaller in the northern part of the simulated domain while the smallest in the northwestern part of China and the central Asia, could also be well simulated (Fig. 1e h and Figs. S4e-S4h). However, the precipitation was overestimated, especially over the northeastern Asia and the southern part of the simulated domain, while underestimated over the northwestern China and the central Asia for both annual and JJA values.

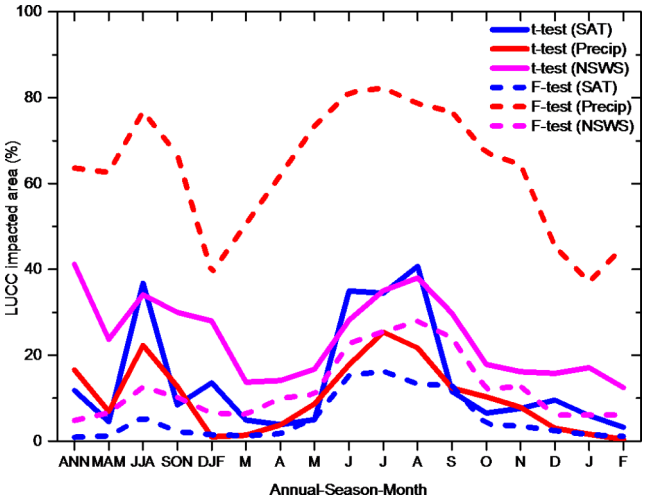

Fig. 2 LUCC impacted terrestrial subregions showing changes in mean state (passing significance t-test at 95% confidence level) and changes in the variability (passing significance F-test at 95% confidence level) for SAT, precipitation (Precip) and near-surface wind speed (NSWS) at annual (ANN), seasonal (MAM: March-April-May; JJA: June-July-August; SON: September-October-November; DJF: December-January-February) and monthly scales

3.2 LUCC impacted terrestrial subregions at annual, seasonal and monthly scales

LUCC impacted terrestrial subregion area for SAT, precipitation and NSWS showing changes in mean state (passing significance t-test at 95% confidence level) and changes in the variability (passing significance F-test at 95% confidence level) at annual, seasonal and monthly scales in 2006–2007 are shown in Fig. 2 and Table S1 in the Supplementary.

For SAT, the impacted terrestrial subregion areas showing changes in mean state were larger than those for changes in the variability at different temporal scales. At annual scale, the impacted subregion area accounted for 11.8% of total simulated terrestrial area for changes in mean state, while 0.9% for changes in the variability. At seasonal scales,

LUCC influenced terrestrial subregion areas in spring, autumn and winter were small, which were 4.5% (1.2%), 8.4% (2.2%) and 13.6% (1.5%) of total simulated terrestrial area for changes in mean state (changes in the variability), respectively. Meanwhile, LUCC influenced terrestrial subregion area in summer for changes in the variability was also small (5.5%). However, the impacted terrestrial subregion area for changes in mean state in summer was much larger (36.8%). For monthly results, LUCC impacted terrestrial subregion areas expressed marked monthly variations. The impacted terrestrial subregion areas were small from March to May, 2006 and September, 2006 to February, 2007 occurred at several dispersed model grids, whereas the influenced subregion areas were larger in June, July and August, which were 35.0% (15.3%), 34.5% (16.3%) and 40.7% (13.3%) for changes in mean state (changes in the variability), respectively.

For the precipitation, the impacted terrestrial subregion areas showing changes in mean state were smaller than those for changes in the variability at different temporal scales. At annual scale, the impacted subregion area accounted for 16.6% of total simulated terrestrial area for changes in mean state, while was much larger (63.6%) for changes in the variability. At seasonal scales, LUCC impacted terrestrial subregion areas expressed marked seasonal characteristics, which were 6.9% (62.6%), 22.3% (76.8%), 12.7% (66.7%), and 1.0% (39.2%) for changes in mean state (changes in the variability) in spring, summer, autumn and winter, respectively. The influenced subregion area in winter was much smaller than those in other seasons, among which the values in summer were the largest. For monthly results, LUCC impacted terrestrial subregion areas expressed marked monthly variations. The influenced terrestrial subregions showing changes in mean state occurred mainly from June to August, whereas those displaying changes in the variability appeared throughout the whole analytzed period. The influenced terrestrial subregion areas in June, July and August were 17.8% (81.2%), 25.4% (82.3%) and 21.7% (78.6%) for changes in mean state (changes in the variability), respectively.

For NSWS, the impacted terrestrial subregion areas showing changes in mean state were larger than those for changes in the variability at different temporal scales. At annual scale, the impacted subregion area accounted for 41.2% of total simulated terrestrial area for changes in mean state, while 4.8% for changes in the variability. At seasonal scales, the influenced terrestrial subregion areas in spring, summer, autumn and winter were close to those for annual results, revealing that seasonal variations for the influenced subregion area of NSWS were small, compared to those for SAT and precipitation. For changes in mean state (changes in the variability), LUCC impacted terrestrial subregion areas were 23.7% (6.6%), 34.1% (12.6%), 30.0% (10.2%) and 28.0% (6.5%) in spring, summer, autumn and winter, respectively. For monthly results, marked monthly variations were detected for the influenced subregion areas. The influenced terrestrial subregion areas in June, July and August were larger, which were 28.2% (22.8%), 35.1% (25.5%), and 38.0% (27.9%) for changes in mean state (changes in the variability), respectively. The influenced terrestrial subregion areas for changes in the variability were comparable to those for changes in mean state in June, July and August, whereas the values for changes in mean state were larger. Meanwhile, monthly variations of the impacted terrestrial subregion areas from NSWS were smaller than those from SAT and the precipitation for both changes in mean state and changes in the variability.

Therefore, for annual result, the impacted subregion areas showing changes in mean state were larger for NSWS and smaller for SAT and the precipitation, whereas the influenced subregion areas showing changes in the variability were much larger for the precipitation and smaller for SAT and NSWS. For seasonal results, the impacted subregion areas were larger for both changes in mean state and changes in the variability in summer, among which changes in the variability for the precipitation were the most pronounced. Furthermore, the influenced subregion areas also displayed marked monthly variations, which were more pronounced from June to August.

3.3 LUCC impacts on terrestrial SAT

At annual scale, spatial distributions of LUCC impacts showed that annual terrestrial SAT generally decreased over East Asia (Fig. 3a). However, limited subregions were detected for SAT changes passing significance t-test or F-test at 95% confidence level, for which terrestrial subregions revealing significant impacts mainly located in the southern and southeastern part of East Asia, showing the increased SAT over the southeastern China, the western part of the Tibet plateau and the northern Indian peninsula (only subregions with significant changes will be investigated in the following sections). For changes in mean state, total annual SAT increased over terrestrial subregions showing significant changes (Fig. 3b), which could be further expressed by PDF distributions of LUCC impacted terrestrial subregion areas for SAT and SAT changes at different grades (Fig. 3c). The probabilities of the influenced terrestrial subregion areas for values smaller than 10 °C between LU80 and LU10 were close, whereas marked differences were detected for SAT larger than 10 °C, which mainly contributed to total SAT change. LUCC induced changes in annual SAT were small (0.27 °C), whereas the averaged terrestrial SAT change intensities over subregions with negative

(-0.85 °C) or positive (0.72 °C) values were much larger. Meanwhile, the impacted subregion areas showing positive SAT changes were larger than those with negative changes, which induced weak positive total SAT change. For changes in the variability, LUCC influenced terrestrial subregion area was much small (0.9%), which could be further expressed by PDF distributions of LUCC impacted terrestrial areas for the averaged SAT and SAT change at different intensities (Fig. 3b and d). Total SAT increased by 0.09 °C over the subregions showing significant changes. However, the averaged terrestrial SAT change intensities over subregions with negative (−0.46 °C) or positive (0.64 °C) values were much larger.

At seasonal scale in summer, SAT increased over the southeastern China and the northeastern India peninsula, while decreased over the northeastern Asia, the western China and the northwestern India peninsula (Fig. 3e). For changes in mean state, SAT change intensities over terrestrial subregions with negative or positive changes were -1.22 °C and 1.12 °C, respectively, whereas total terrestrial SAT change was much smaller (−0.40 °C), which mainly resulted from the larger impacted subregions showing negative changes (Fig. 3f g). There was good consistence for the influenced terrestrial subregion areas for SAT smaller than 10 °C shown by PDF distributions, whereas larger differences were detected for SAT larger than 10 °C, which mainly contributed to negative SAT change. For changes in the variability in summer (Fig. 3f h), LUCC influenced terrestrial subregion area was small (5.5%). Terrestrial SAT change was small (−0.33 °C) over the studied domain, whereas SAT change intensities over terrestrial subregions with negative (−1.17 °C) or positive (0.74 °C) changes were larger.

At monthly scale in June, July and August (Fig. 3i and t), LUCC influenced terrestrial subregion areas were larger than those in summer. For changes in mean state, marked monthly variations were detected. In June (August), the impacted subregions showing negative SAT changes were larger (smaller) than those with positive changes. In July, the impacted subregions showing negative SAT changes were close to those with positive changes. Total SAT changes were negative in June (-1.24 °C) and July (−0.47 °C), while positive in August (0.49 °C). However, SAT change intensities over terrestrial subregions with negative or positive values were larger, which were −1.77 °C~−1.28 °C and 1.28 °C ~ 1.71 °C, respectively. PDF distributions of the influenced terrestrial subregion areas for the averaged SAT in June, July and August were similar to those in summer, showing larger differences for SAT larger than 10 °C. For changes in the variability, LUCC influenced terrestrial subregion areas were small in June (15.3%), July (16.3%) and August (13.3%), respectively. Terrestrial SAT changes varied in June, July and August, which were −0.49 °C, 0.02 °C, and −0.03 °C, respectively. However, SAT change intensities over terrestrial subregions with negative (−1.34 °C~−1.03 °C) or positive (0.98 °C ~ 1.16 °C) values were larger.

Therefore, LUCC influenced terrestrial subregion areas at different temporal scales for SAT changes in mean state were larger than those for changes in the variability. LUCC impacts on terrestrial SAT for both the influenced terrestrial subregions and change intensities were larger at monthly scales, compared to those at annual and seasonal scales, especially for annual results. Similar PDF distributions of the influenced terrestrial subregion areas for the simulated SAT between LU80 and LU10 were found at different temporal scales. However, differences were detected for various SAT grades, especially for SAT larger than 10 °C, which mainly contributed to total SAT changes. Total terrestrial SAT changes were small at different temporal scales, whereas SAT change intensities over terrestrial subregions with negative or positive values were larger.

3.4 LUCC impacts on the precipitation

At annual scale, LUCC impacts on the precipitation were much more complicated than those for changes in SAT for both the impacted terrestrial subregions and spatial distributions of subregions with positive or negative changes, which were more pronounced over the EAM region showing the increased in the north while the decreased in the south (Fig. 4a). LUCC impacted terrestrial subregion area for changes in mean state of the precipitation was little larger than those for SAT, whereas the value for changes in the variability of the precipitation was much larger than those for SAT (Figs. 3b and 4b). The probabilities of the simulated precipitation between LU80 and LU10 were close for both changes in mean state and changes in the variability, which displayed nearly symmetrical distributions between positive and negative changes (Fig. 4c and d). For changes in mean state/changes in the variability, total terrestrial precipitation changes were small (-0.03 mm day^{-1}/−0.02 mm day^{-1}), whereas the precipitation change intensities over terrestrial subregions with negative (−0.95 mm day^{-1}/−0.48 mm day^{-1}) or positive (0.84 mm day^{-1}/0.43 mm day^{-1}) values were larger.

At seasonal scale in summer, spatial distributions of LUCC influenced terrestrial subregions of the precipitation were similar to those for annual results (Fig. 4e). Total terrestrial precipitation for changes in mean state (-0.23 mm day^{-1}) and changes in the variability (−0.10 mm day^{-1}), resulting from nearly symmetrical positive and negative changes, were small. However, change intensities over terrestrial subregions with negative (−3.00 mm day^{-1}/−1.50 mm

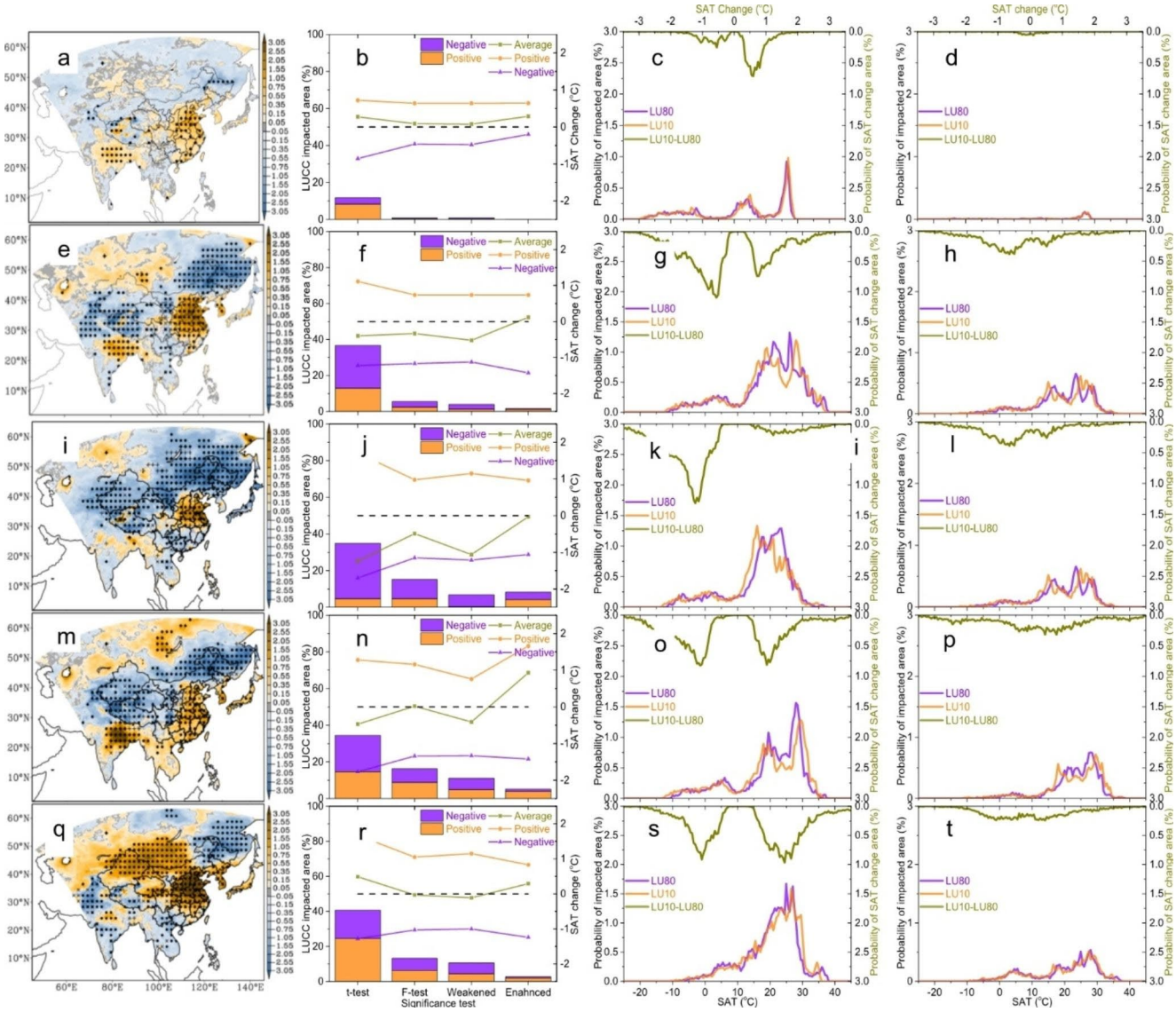

Fig. 3 LUCC induced SAT changes at (**a-d**) annual, (**e-h**) seasonal (JJA), and (**i-t**) monthly (June: **i-l**, July: **m-p**, August: **q-t**) scales. (**a, e, i, m, q**) Spatial distributions of LUCC impacted SAT changes, within which symbol '●' indicates subregions passing significance t-test at 95% confidence level (changes in mean state), and symbols '×/+' denote subregions passing significance F-test at 95% confidence level showing the weakened/enhanced variability, respectively (changes in the variability). (**b, f, j, n, r**) LUCC impacted terrestrial subregion areas (stack column) passing significance t-test or F-test and those showing the weakened or enhanced variability, as well as changes in the averaged SAT (line and symbol, dash line '-' for zero value line). (c/d, g/h, k/l, o/p, s/t) PDF distributions of LUCC impacted terrestrial subregion areas for the averaged SAT (blue and red line)/PDF distributions of the influenced terrestrial subregion areas for SAT changes (dark yellow line) at different grades passing significance t-test/F-test (units: °C)

day^{-1}) or positive (2.31 mm day^{-1}/1.19 mm day^{-1}) values were larger for changes in mean state/changes in the variability, showing that change intensities from the former were stronger (Fig. 4f). LUCC impacted terrestrial subregion area for changes in mean state was small, whereas the value for changes in the variability was much larger, for which both the weakened and the enhanced variability were pronounced. Meanwhile, the probability for LUCC induced both changes in mean state and changes in the variability were larger for the intensity between 2 mm day^{-1} to 5 mm day^{-1} (Fig. 4 g and 4 h), which mainly contributed to changes in the precipitation.

At monthly scales in June, July and August (Fig. 4i and t), changes in the precipitation displayed marked monthly variations. For LUCC impacts on changes in mean state/changes in the variability, the precipitation changes were 0.13 mm day^{-1}/-0.06 mm day^{-1}, −1.14 mm day^{-1}/−0.38 mm day^{-1}, 0.11 mm day^{-1}/0.07 mm day^{-1} in June, July and August, respectively, which resulted from nealy symmetrical positive and negative changes, especially for changes in the

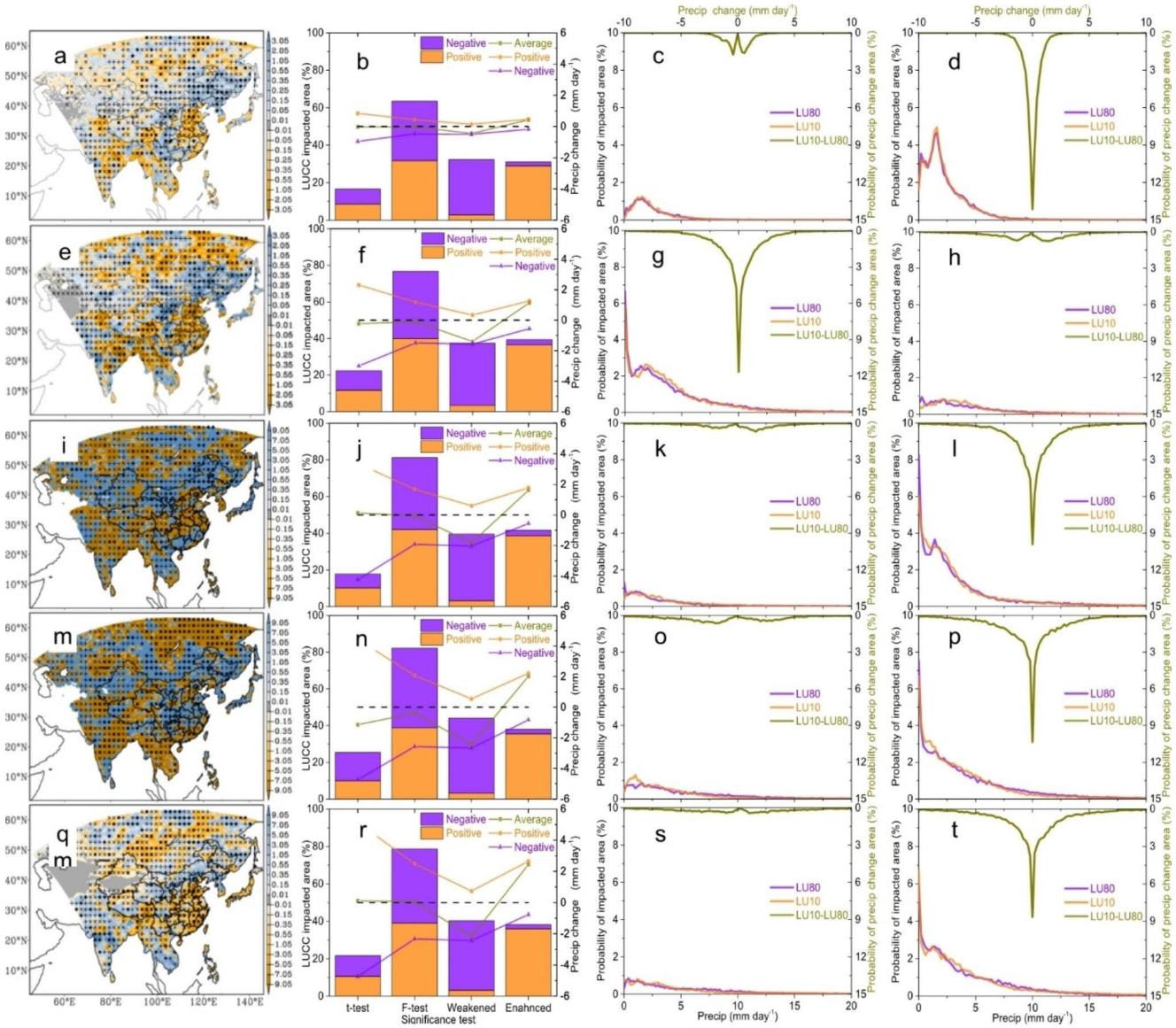

Fig. 4 Same as Fig. 3, but for LUCC induced changes in the precipitation (units: mm day^{-1})

variability. However, LUCC impacted change intensity of the precipitation over terrestrial subregions with negative (−4.74 mm day^{-1} ~−4.23 mm day^{-1}/−2.57 mm day^{-1} ~−1.92 mm day^{-1}) or positive (3.36 mm day^{-1} ~5.13 mm day^{-1}/1.68 mm day^{-1} ~2.49 mm day^{-1}) values were larger for changes in mean state/changes in the variability. The probabilities for the influenced terrestrial subregion areas in June, July and August were similar to those in summer for both changes in mean state and changes in the variability, showing larger differences for the precipitation between 2 mm day^{-1} to 5 mm day^{-1}, which were consistent with total precipitation changes.

As a result, LUCC influenced terrestrial subregions for changes in mean state were small, whereas the values for changes in the variability were much larger, for which both the weakened and the enhanced variability were pronounced. LUCC impacts on terrestrial precipitation were larger at monthly scales (June, July and August), compared to those at annual and seasonal scales, especially for annual results. Furthermore, the weakened (enhanced) variability was mainly corresponding to the decreased (enhanced) precipitation, which resulted in small change in total precipitation. Though LUCC impacted total precipitation for both changes in mean state and changes in the variability were small, changes in the precipitation intensities over terrestrial subregions with negative or positive values for the former were stronger.

3.5 LUCC impacts on NSWS

At annual scale, spatial distributions of LUCC impacted terrestrial subregions for NSWS showed that the influences appeared across the whole East Asia, which were more pronounced over the EAM region showing the decreased in the south and the increased in the north (Fig. 5a). For changes in mean state, total NSWS change was small (0.03 m s^{-1}), whereas the corresponding changes over terrestrial subregions with negative/positive values were larger (-0.27 m s^{-1}/0.29 m s^{-1}), which could be well interpreted by nearly symmetric distributions of the probabilities for LUCC impacted subregions with negative or positive NSWS changes (Fig. 5b and c). The probability of LUCC impacted terrestrial subregion area increased for the strong NSWS, while decreased for the medium and weak intensity from LU80 to LU10, whereas the influenced subregion area for the medium intensity of NSWS decreased. For changes in the variability, the probabilities of LUCC influenced terrestrial subregion areas were small and negligible (Fig. 5b and d). Total NSWS change was small (0.16 m s^{-1}), whereas the corresponding change intensity of NSWS over terrestrial subregions with negative (−0.64 m s^{-1}) and positive (0.66 m s^{-1}) values were larger.

At seasonal scale in summer, spatial distributions of LUCC induced NSWS changes were similar to those for annual results (Fig. 5e). For changes in mean state (Fig. 5f g), total NSWS change over terrestrial subregions was small (0.06 m s^{-1}), which resulted from nearly symmetrical positive (-0.36 m s^{-1}) and negative (0.41 m s^{-1}) changes, respectively. The probability distributions revealed similar characteristics to those for annual results, showing the increased terrestrial subregion area for the strong NSWS while the decreased one for the weak and medium ones, especially for the medium NSWS intensity, which resulted in symmetric probability distributions of LUCC impacted terrestrial subregions with negative or positive changes. The impacted terrestrial subregion area for changes in the variability in summer, which was smaller than those for changes in mean state, was larger than those for annual results and could not be neglected (Fig. 5h). For changes in the variability, total terrestrial NSWS change was small (0.15 m s^{-1}), which resulted from the larger impacted subregion areas showing positive changes (0.38 m s^{-1}) than those showing negative changes (−0.35 m s^{-1}). The probability distributions for changes in the variability revealed asymmetric probability distributions of LUCC impacted terrestrial subregions with negative or positive changes.

At monthly scales in June, July and August (Fig. 5i and t), spatial distributions of LUCC impacts on NSWS displayed marked monthly variations. For changes in mean state, total NSWS changes were 0.37 m s^{-1}, 0.16 m s^{-1} and -0.28 m s^{-1} in June, July and August, respectively. However, LUCC impacted change intensity of NSWS over terrestrial subregions with negative (−0.62 m s^{-1}~−0.54 m s^{-1}) or positive (0.59 ~ 0.67 m s^{-1}) values were larger. In June and July (August), the impacted subregion areas showing positive NSWS changes were larger (smaller) than those with positive changes. For changes in the variability, total NSWS changes were 0.32 m s^{-1}, 0.08 m s^{-1} and −0.24 m s^{-1} in June, July and August, respectively. However, NSWS change intensities over terrestrial subregions with negative (−0.51 m s^{-1}~−0.31 m s^{-1}) or positive (0.40 m s^{-1}~0.56 m s^{-1}) values were larger. In June and July (August), the impacted subregion areas showing positive changes were larger (smaller) than those with positive changes. The probability distributions for both changes in mean state and changes in the variability showed marked monthly variations. In June, the impacted terrestrial subregion area decreased for the weak and medium intensity of NSWS while increased for the medium-strong one. In July, the influenced terrestrial subregion area increased for the weak and strong intensity of NSWS while decreased for the medium ones. In August, the impacted terrestrial subregion area increased for the weak intensity of NSWS while decreased for the medium and strong ones. Therefore, for both changes in mean state and changes in the variability, the asymmetric distributions of the probability for LUCC impacted terrestrial subregions showing negative or positive changes in June, July and August resulted in larger total NSWS changes than those for annual and seasonal results, with the exception of the smaller values for changes in the variability in July.

As a result, LUCC impacts on total NSWS for both changes in mean state and changes in the variability were small, whereas NSWS changes over terrestrial subregions with positive or negative changes were larger. LUCC induced NSWS changes for seasonal (summer) and monthly results (June, July and August) were larger than those for annual results, especially for monthly results. The influenced terrestrial subregions for changes in the variability were comparable to those for changes in mean state for summer and monthly results. PDF distributions of LUCC impacted NSWS for changes in mean state and changes in the variability in summer were similar to those for annual results. However, marked differences were detected among PDF distributions of NSWS changes in June, July and August, which were different from those for annual and summer results. For annual results, the symmetric distributions of NSWS change probability over LUCC impacted subregions with negative or positive changes resulted in small total NSWS changes for both changes in mean state and changes in the variability. For summer results, the symmetric distributions of NSWS change probability over LUCC impacted

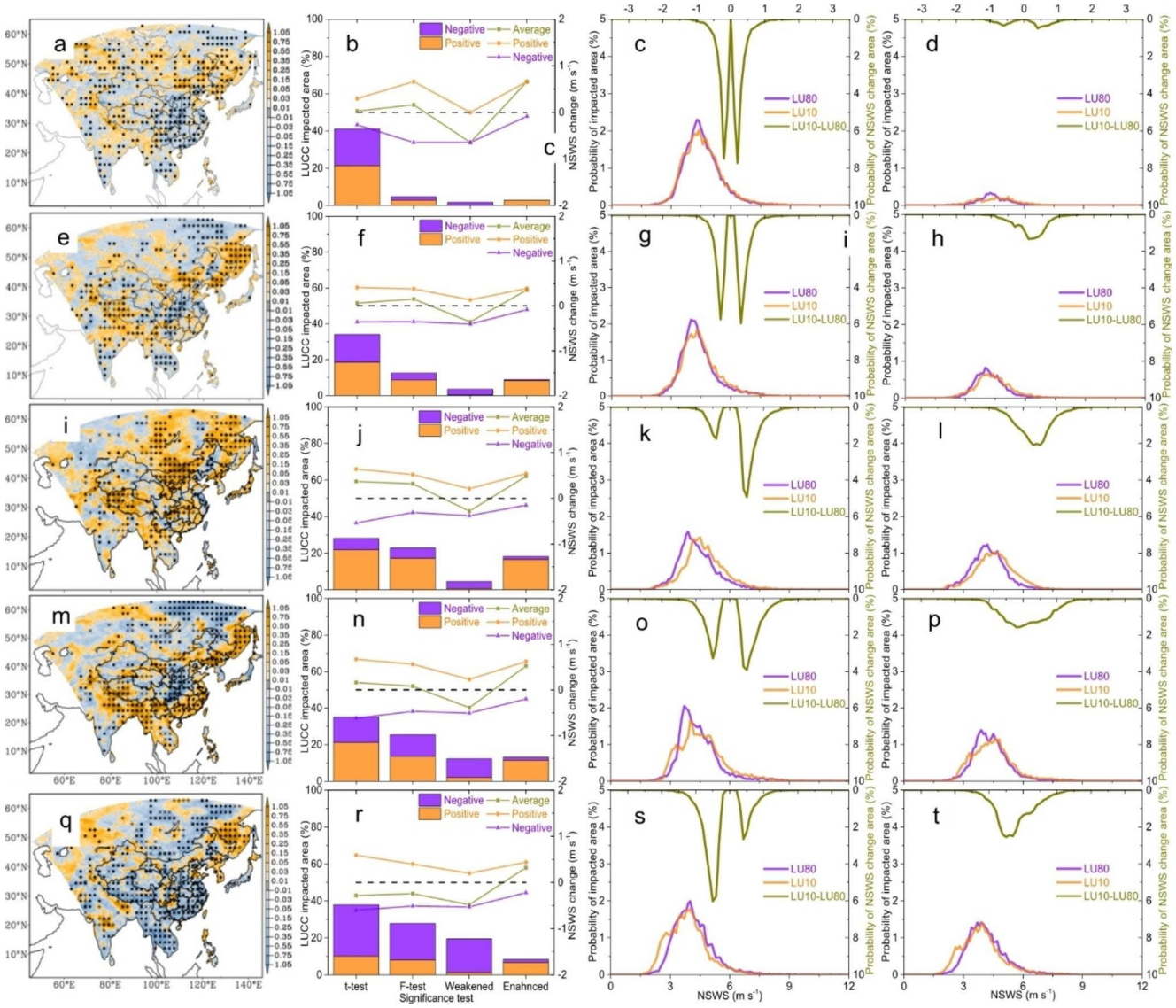

Fig. 5 Same as Fig. 3, but for LUCC induced changes in the near-surface wind speed (NSWS, units: m s^{-1})

subregions with negative or positive changes for changes in mean state while asymmetric distributions for changes in the variability resulted in smaller change for the former and larger one for the latter. For monthly results, the asymmetric distributions of NSWS change probability for LUCC impacted terrestrial subregions with negative or positive changes resulted in larger total NSWS changes for both changes in mean state and changes in the variability, with the exception in July.

4 Discussions

As LUCC impacts on SAT, precipitation and NSWS were more pronounced in summer over the eastern China, which locates over the EAM region, physical mechanisms in interpreting LUCC impacts on East Asian summer monsoon (EASM) system are to be detailed explored.

4.1 LUCC influences on radiation budget

Spatial distributions of LUCC induced radiative forcing at top of atmosphere (RFT, Fig. 6a) were similar to those for changes in SAT over the EASM region in summer (Fig. 3e). RFT was positive (negative) in the south (north), which resulted from larger increased (decreased) net shortwave (Fig. 6b) and smaller decreased (increased) net longwave radiation flux (Fig. 6c), respectively. Changes in radiation flux at top of atmosphere can be further interpreted by changes in radiation budget at surface, for which spatial distributions of LUCC induced changes in net shortwave and

longwave radiation flux at surface were similar to those at top of atmosphere over the EASM region.

For LUCC impacts on shortwave radiation flux at surface over the EASM region (Fig. 6d and f), spatial distributions of changes in downward component were similar to those of net shortwave radiation flux. Changes in upward component, showing much weaker intensity than changes in downward component, were generally negative excepting for the the increased over the north China plain. The larger increased downward component and the smaller changed upward component contributed to the increased net shortwave radiation flux in the south. However, the larger decreased downward component and the smaller decreased upward component resulted in the decreased net shortwave radiation flux in the north. For LUCC influences on longwave radiation flux at surface over the EASM region (Fig. 6 g-6i), the smaller increased downward component and the larger increased upward component contributed to the decreased net longwave radiative flux in the south. However, the smaller changed downward component and the larger decreased upward component resulted in the increased net longwave radiation flux in the north.

As a total, the larger increased (decreased) net shortwave radiation flux and the smaller decreased (increased) net longwave radiation flux contributed to the increased (decreased) radiative forcing at surface (RFS) in the south (north) over the EASM region (Fig. 6j). Accordingly, spatial distributions of changes in the sensible heat flux were consistent with those for RFS over the EASM region (Fig. 6k), whereas changes in latent heat flux were generally positive, showing the increased in both the south and the north of the EASM region (Fig. 6l), which were consistent with changes in surface evaporation and local moisture flux (Fig. 7a).

4.2 LUCC impacts on surface albedo and roughness length

Spatial distributions of both RFT and RFS were similar to those of downward shortwave component changes over the EASM region, showing that LUCC induced changes in downward shortwave radiation flux at surface were more pronounced among different radiation components. Changes in upward shortwave radiation flux at surface were determined by changes in downward shortwave component and surface albedo. LUCC induced changes in surface albedo displayed the decreased in the south and increased in the north over the EASM region (Fig. 7b). The decreased (increased) surface albedo were originally thought to result in the decreased (increased) upward shortwave component in the south (north) over the EASM region, whereas LUCC induced changes in upward shortwave component were generally contrary to the assumed. The contributions to upward shortwave component changes from changes in downward shortwave component were larger than those from changes in surface albedo. Therefore, changes in net

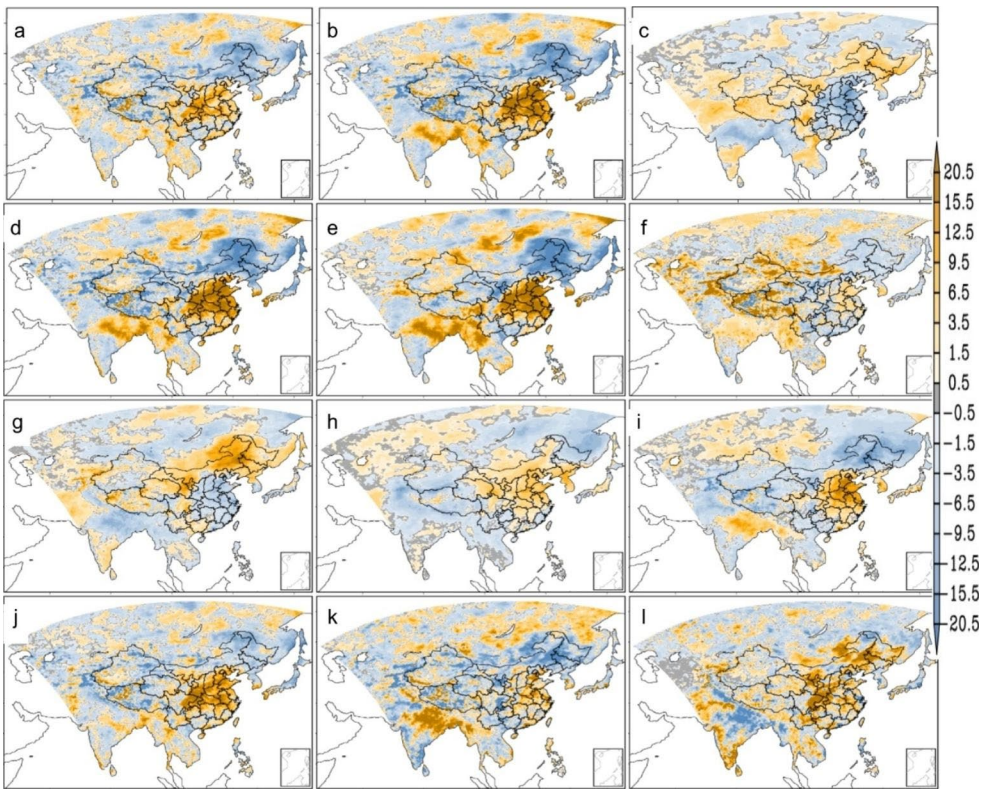

Fig. 6 LUCC induced **(a)** radiative forcing (RFT), changes in net **(b)** shortwave and **(c)** longwave radiative flux at top of atmosphere in summer. Changes in (**d, g**) net radiation flux, (**e, h**) downward and (**f, i**) upward components of (**d-f**) shortwave and (**g-i**) longwave radiation flux at surface in summer. LUCC induced (**j**) radiative forcing at surface (RFS), changes in (**k**) sensible and (**l**) latent heat flux in summer (units: W m^{-2})

shortwave radiation flux could not be directly interpreted by LUCC induced changes in surface albedo.

Spatial distributions of LUCC impacts on surface roughness length over the EASM region are shown in Fig. 7c, showing the increased in the south while the decreased in the north, which contributed to the decreased NSWS in the south while the increased in the north.

4.3 LUCC influences on cloud amount

LUCC impacts on low, middle and high cloud amounts are shown in Fig. 7d, and Figs. S5a-S5b in the Supplementary. The cloud amount at different levels consistently decreased in the south and increased in the north over the EASM region, especially for low cloud amount, which resulted in similar changes in total cloud amount. Accordingly, the cloud ceiling increased in the south and decreased in the north over the EASM region (Fig. 7e). Pressure–latitudinal (longitudinal) cross-sections along the 120° E, 35° N and 45° N axes for LUCC induced changes in cloud amount in summer clearly revealed that the decreased low, middle and high level cloud amounts and the increased cloud ceiling in the south, while opposite changes in the north over the EASM region (see Supplementary Figs. S5c-S5e).

For LUCC impacts on surface energy budget in the southern part of the EASM region, the decreased cloud amount contributed to the increased downward shortwave radiation flux. Though surface albedo decreased, the upward shortwave radiation flux also increased, because the contributions to changes in upward shortwave radiation flux from the increased downward radiation component were larger than those from the decreased surface albedo. The increased downward shortwave component was much larger than the increased upward component for both the the intensity and covered areas, which resulted in the increased net shortwave radiation flux. Meanwhile, the downward longwave radiation flux increased due to the increased upward longwave radiation flux, though cloud amount decreased and cloud ceiling increased. Therefore, the smaller increased downward component and the larger increased upward components resulted in the decreased net longwave radiation flux.

For LUCC impacts on surface energy budget in the northern part of the EASM region, the increased cloud amount contributed to the decreased downward shortwave radiation flux. The contributions to changes in upward shortwave radiation flux from changes in downward shortwave component were larger than those from the increased surface albedo. The upward shortwave radiation flux also decreased, though surface albedo increased. The decreased downward shortwave radiation component was much larger than the decreased upward radiation component for both the the intensity and covered areas, which resulted in the decreased net shortwave radiation flux. Meanwhile, changes in the downward longwave radiation flux were small, which can be attributed to the combined affections from the decreased upward longwave radiation flux, the increased cloud amount and decreased cloud ceiling. Therefore, the smaller changed downward component and the larger decreased upward components resulted in the increased net longwave radiation flux.

Therefore, SAT increased (decreased) in the southern (northern) part of the EASM region in summer, which could be interpreted mainly by changes in downward shortwave radiation flux through the land use-cloud-radiation feedback, within which changes in cloud amount played an important role in alerting radiation budget. Meanwhile, changes in the planet boundary layer displayed positive (negative) values in the south (north), which shared similar spatial distributions as those for changes in SAT (Figs. 3e and 7f).

4.4 LUCC induced changes in the EASM circulation and moisture flux

LUCC influences displayed consistently increased surface evaporation over the EASM region in summer, which was different from those of changes in the precipitation. Therefore, LUCC impacts on the EASM circulation and moisture flux are to be explored.

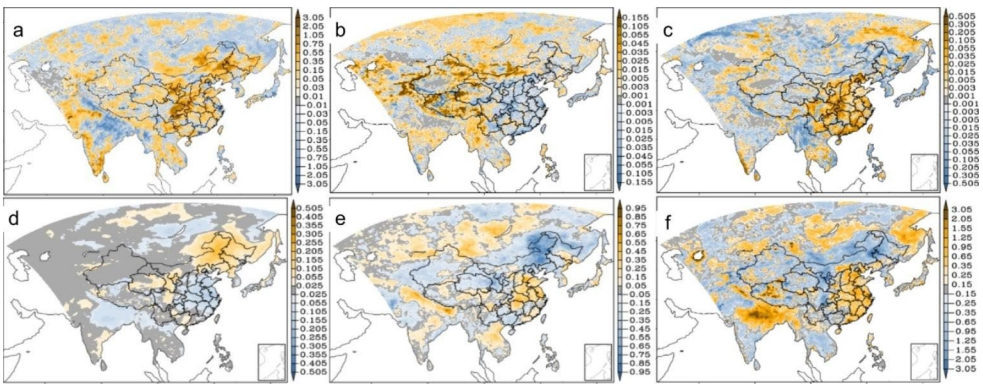

Fig. 7 LUCC induced changes in **(a)** surface evaporation (unit: mm day^{-1}), **(b)** surface albedo, **(c)** roughness length (unit: m), **(d)** low cloud amount, **(e)** cloud ceiling (unit: 10^{3} m), and **(f)** planetary boundary layer height (unit: 10^{2} m) in summer

LUCC impacts on the zonal winds at 700 hPa displayed marked subregional characteristics from the south to the north over the EASM region (Fig. 8a, and Fig. S6a in the Supplementary). In the lower latitude, the easterly winds intensified in the eastern part. In the western part, the westerly winds strengthened along the southern boundary of the Tibet Plateau while weakened to the south of the Tibet Plateau. In the low-mid latitude, the westerly winds generally weakened. In the mid-high latitude, the westerly winds weakened (strengthened) in the western part, and strengthened (weakened) to the south (north) of 50°N in the eastern part. Changes in the meridional winds at 700 hPa are shown in Fig. 8b and Fig. S6b in the Supplementary. LUCC impacts on the meridional winds mainly displayed the strengthened southerly winds in the south, while the enhanced northerly winds and the weakened southerly winds in the north over the EASM region. Meanwhile, the southerly winds weakened along the seashore of southeastern China, as well as the southern boundary of the Tibet Plateau.

Spatial distributions of changes in total wind speed and vector and moisture flux at 700 hPa over the EASM region were shown in Fig. 8c and d, and Figs. S6c-S6d in the Supplementary, which shared similar spatial characteristics. In the low-mid latitude, the enhanced southeasterly moisture flux from the northwestern Pacific, the intensified southerly branch from the south China sea, and the amplified southwesterly branch along the southern boundary of the Tibet Plateau contributed to the strengthened moisture flux to be transported to the northern part of the EASM region, though the southwesterly branch weakened along the northern Indian peninsula, Bay of Bengal and the northern Indo-China peninsula. In the mid-high latitude, changes in the westerly moisture flux displayed contrary distributions to the south/north of 50°N. The westerly moisture flux weakened/enhanced to the west/east of the Lake Baikal for the former, while the opposite characteristics for the latter. These distributions resulted in the altered wind shear near the 50°N axis, for which the westerly water vapor transportation to the north of 50°N was obstructed. Combined with the weakened/strengthened westerly moisture flux to the west/east of the Lake Baikal to the south of 50°N, the northerly moisture flux to the northeast Asia strengthened. Spatial distributions of changes in the moisture flux across the whole troposphere were similar to those at 700 hPa (Fig. 8e, and Fig. S6e in the Supplementary). More water vapor was transported to the northeast Asia from both the southerly moisture flux and the westerly water vapor transportation. Meanwhile, moisture flux in the southern part of the EASM region weakened. Therefore, the precipitation was affected not only by LUCC induced the increased local evaporation related moisture flux over both the southern and the northern part of the EASM region, but also by LUCC impacts on the EASM circulation related moisture flux. Changes in the precipitation could not be solely interpreted by changes in local surface evaporation, for which LUCC impacted moisture flux played an important role.

Spatial distributions of subtropical westerly jet and the corresponding changes at 200 hPa are shown in Fig. 8f and Fig. S6f in the Supplementary. Changes in the subtropical westerly jet near the jet axis displayed negative-positive characteristics over the EASM region, showing the westerly jet axis inclined to the northeast Asia. The westerly jet displayed the weakened/intensified to the south/north of the axis, which was in accordance with the enhanced EASM circulation and moisture flux, and the increased precipitation over the northeast Asia (Zhao 2013).

4.5 LUCC impacts on the vertical characteristics

LUCC impacts on the EASM circulation and moisture flux can be further explained by pressure–latitudinal cross-sections along the 120° E axis for changes in the zonal,

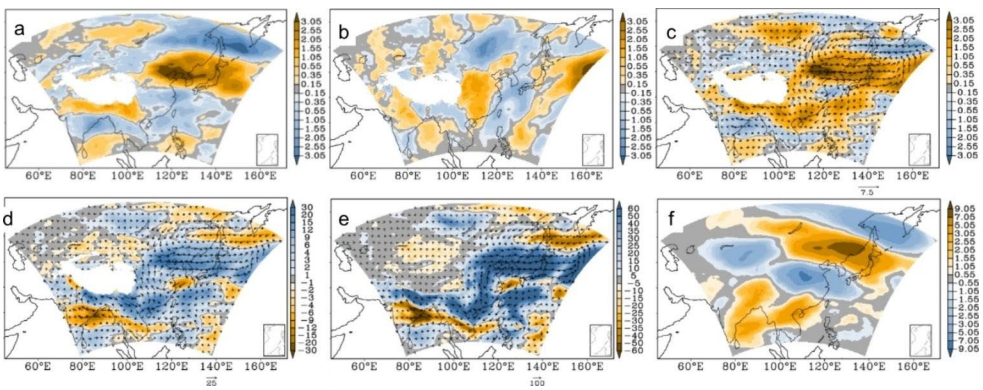

Fig. 8 Spatial distributions of LUCC induced changes in **(a)** the zonal winds at 700 hPa (unit: m s^{-1}), **(b)** the meridional winds at 700 hPa (unit: m s^{-1}), **(c)** wind speed (shaded) and vector at 700 hPa (unit: m s^{-1}), **(d)** moisture flux (shaded) and vector at 700 hPa (unit: 10^{-3} kg hPa^{-1} m^{-1} s^{-1}), **(e)** moisture flux (shaded) and vector across the whole troposphere (unit: 10^{-3} kg hPa^{-1} m^{-1} s^{-1}), and **(f)** the westerly wind speed at 200 hPa (units: m s^{-1}) in summer (**a-d**: white subregions for topography above 700 hPa)

meridional and total winds (Fig. 9a and Fig. S7 in the Supplementary). Changes in the zonal and meridional winds displayed similar vertical characteristics over the EASM region, showing the negative-positive-negative distributions from the south to the north, whereas differences for the vertical characteristics were detected. In the lower latitude, changes in the zonal winds mainly expressed the increased easterly winds in the low-middle troposphere while the decreased easterly winds in the mid-high troposphere. In the middle latitude, changes in the zonal winds mainly showed the decreased (increased) westerly winds to the south (north) of nearly 35° N. In the mid-high latitude, changes in the zonal winds mainly displayed the decreased westerly winds. Changes in the zonal winds showing positive values inclined northward from middle to mid-high latitude, which was consistent with changes in the westerly jet axis shown by Fig. 8f. In the mid-high troposphere, changes in the meridional winds displayed as the decreased northerly winds in the south while the decreased southerly winds in the north. In the low-mid troposphere, it was the decreased southerly winds in the lower latitude and the increased southerly winds in the mid latitude. In the mid-high latitude, it was the decreased southerly winds to the north of 48°N while the increased northerly winds to the south of 48°N, with the exception of the decreased southerly winds in the lower layer. Consequently, changes in the total winds occurred across the whole troposphere, showing similar vertical distributions to those from changes in zonal winds.

Changes in EASM circulation related moisture flux could be revealed by pressure–latitudinal cross-sections along the 120° E axis of the averaged zonal, meridional and total moisture flux and the corresponding changes (Fig. 9b and Fig. S8 in the Supplementary), which shared similar distributions to those from the EASM circulation. However, the influenced moisture flux mainly concentrated on the low-mid troposphere, which had a considerable impact on the water vapor transportation over the EASM region. Changes in the moisture flux were generally consistent from the bottom to the middle troposphere, with the exception of changes over near surface layers.

Pressure–latitudinal cross-sections along the 120° E axis for changes in relative humidity and water vapor mixing ratio are displayed in Fig. 9c and d. The relative humidity generally decreased with the exception of the increased to the north of 40°N in the lower troposphere. The vertical distribution of water vapor mixing ratio was similar to those for relative humidity, whereas water vapor mixing ratio increased between 35°N and 45°N in the low-mid troposphere. With the enhanced EASM circulation, more water vapor was transported to the northern part of the EASM region. Both the strengthened EASM related moisture flux and the increased local evaporation contributed to the increased relative humidity and water vapor mixing ratio in the northern part of the EASM region. Meanwhile, the weakened EASM moisture flux (larger) and the increased local evaporation (smaller) resulted in the decreased relative humidity in the southern part of the EASM region. However, changes in water vapor mixing ratio (increased) were contrary to changes in relative humidity (decreased) between 30°N and 40°N in the lower troposphere, which could be attributed to LUCC induced changes in SAT, shown by Fig. 3e. With the increased SAT between 30°N and 40°N, the saturated water vapor pressure enlarged, for which more water vapor was expected with an increase in water vapor mixing ratio but a decrease in relative humidity.

4.6 How EASM circulation was affected?

Changes in the southerly winds over the EASM region could be interpreted by LUCC induced changes in sea level pressure (SLP) in summer shown by Fig. 10a and b. SLP decreased from the southwestern China to the northeastern China, while increased over the southern China. SLP differences between the southern China and the northern China increased, which were beneficial to the increased pressure gradient. These distributions contributed to the strengthened southeasterly winds from the northwestern Pacific subtropical high, the intensified southerly winds from the South China Sea, and the enhanced southwesterly winds along the southern boundary of the Tibet Plateau. Therefore, more moisture flux from the ocean was transported to

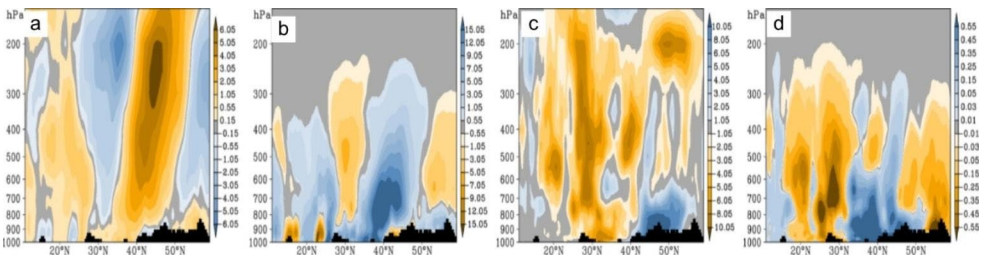

Fig. 9 Pressure–latitudinal cross-sections along the 120° E axis (black area for topography) of LUCC induced changes in **(a)** total wind speed (unit: m s^{-1}), **(b)** moisture flux (unit: 10^{-3} kg hPa^{-1} m^{-1} s^{-1}), **(c)** relative humidity (unit: %), and **(d)** water vapor mixing ratio (unit: 10^{-3} kg kg^{-1}) in summer

the northeast Asia, which contributed to contrary changes in the precipitation for both the covered subregions and the intensity between the southern and the northern part of the EASM region.

Pressure–latitudinal cross-sections along the 120° E axis for changes in the temperature field across the troposphere are displayed in Fig. 10c. Temperature gradient was altered due to the increased temperature in the low-mid latitude and the decreased in the mid-high latitudes, which resulted in changes in temperature advection. The increased temperature gradient in the mid-high latitudes while the decreased in the low-mid latitudes induced the enhanced westerly winds in the north (to the south of 50°N) and the weakened in the south over the EASM region.

LUCC impacts on the westerly winds in the high latitude (to the north of 50°N) displayed different changes to the west/east of the Lake Baikal (Fig. 8a), which could be interpreted by pressure–longitudinal cross-sections along the 45° N/55° N axes for changes in the temperature fields (Fig. 10d and e). Changes in temperature field expressed the negative-positive-negative differences from the west to the east along the 45° N axis, which resulted in the decreased temperature gradient in the west while the increased in the east, and then the weakened westerly in the west and the enhanced in the east. However, changes in temperature field revealed the positive-negative differences from the west to the east along the 55° N axis, which resulted in the increased temperature gradient in the west and the decreased in the east, and then the intensified westerly in the west while the weakened in the east.

Pressure–latitudinal cross-sections along the 120° N axis for changes in vertical velocity fields are displayed in Fig. S9 in the Supplementary, with which the weakened/strengthened vertical motions can be well displayed. The vertical motion generally weakened (enhanced) to the south (north) 40°N over the EASM region, with which the convection activities were inhabited (promoted) and the precipitation were subsequently dampened (strengthened) in the south (north).

5 Conclusions

The impacts of LUCC on regional climate were explored using the WRF model with Noah-mosaic approach, with which subgrid scale process of the LUCC could be well represented. LUCC impacts on SAT, precipitation and NSWS displayed marked temporal and spatial characteristics. At annual scale, LUCC influenced terrestrial subregions were small. For seasonal results, LUCC impacted terrestrial subregions displayed marked seasonal characteristics, which were larger in summer. The results from monthly variations further confirmed greater LUCC impacted terrestrial subregions over summer time, whereas the influenced terrestrial subregions in certain months were also notable. LUCC impacts on SAT and NSWS at different temporal scales mainly presented as changes in mean state, whereas LUCC influenced precipitation mainly displayed as changes in the variability. LUCC induced changes in the averaged SAT, precipitation and NSWS for changes in mean state and changes in the variability were small, whereas the nearly symmetric distributions between positive and negative changes, which contributed to total changes, were much larger and might have a considerable impact on local and regional climate, especially on extreme climate events. Therefore, the LUCC climate effects for both the influenced

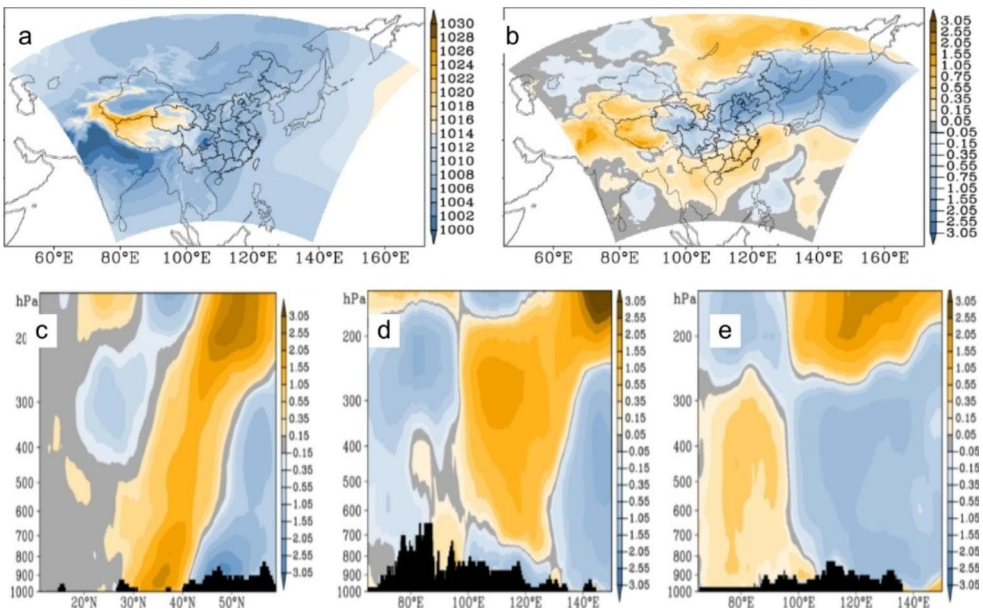

Fig. 10 **(a)** The averaged and **(b)** LUCC induced changes in sea level pressure in summer (unit: hPa). **(c)** Pressure–latitudinal cross-sections along the 120° E axis (black area for topography) of LUCC induced changes in temperature field in summer (unit: °C). (d-e) Pressure–longitudinal cross-sections along the **(d)** 45° N and **(e)** 55° N axes of LUCC induced changes in temperature fields in summer (units: °C)

terrestrial subregions and the intensity were larger over summertime, which expressed marked affection on the East Asian Summer Monsoon system.

LUCC's direct impacts on regional climate can be attributed to changes in surface albedo and surface roughness length, whereas the land use-cloud-radiation feedback played an essential role in radiation budget changes, and then altered SAT, precipitation and NSWS. In the northern part of the EASM region, surface roughness length decreased, which mainly resulted in the increased NSWS. Meanwhile, surface albedo increased, which contributed to the decreased RFS and SAT. The sensible heat flux decreased while the latent heat flux increased. However, the decreased RFS could not be directly interpreted by LUCC impacted surface albedo. With the enhanced EASM circulation and moisture flux, more water vapor was transported to the northeast Asia. Meanwhile, local evaporation also enhanced. Moisture flux from both EASM related circulation and local evaporation contributed to an increase in the relative humidity, which were beneficial to the increased precipitation with the common affections of the intensified vertical motions. The cloud amount increased and cloud ceiling decreased, from which downward shortwave radiation flux obviously decreased and mainly contributed to the decreased RFS. The upward shortwave radiation flux slightly decreased because the influences from the intense decreased downward shortwave radiation flux were larger than those from the increased surface albedo. However, in the southern part of the EASM region, surface roughness length increased, which mainly resulted in the decreased NSWS. Meanwhile, surface albedo decreased, which contributed to the increased RFS and SAT. The sensible heat flux increased while the latent heat flux also increased. The decreased RFS could not be directly interpreted by LUCC impacted surface albedo. With the enhanced EASM circulation and moisture flux, more water vapor was transported to the northern part of EASM region. Meanwhile, latent heat flux increased due to the increased SAT and the enlarged saturated water vapor pressure, for which more water vapor was expected. The larger decreased EASM related moisture flux and the smaller increased local evaporation contributed to a decrease in the relative humidity, which were beneficial to the decreased precipitation with common affection of the dampened vertical motions. The cloud amount decreased and cloud ceiling increased, from which downward shortwave radiation flux obviously increased and mainly contributed to the increased RFS. Therefore, the upward shortwave radiation flux slightly changed because the influences from the intense increased downward shortwave radiation flux were larger than those from the decreased surface albedo.

Therefore, the land use-cloud-radiation feedback played an important role in LUCC impacts on radiation budget, which had marked impacts on energy and water cycle, and then local and regional climate. There are still many uncertainties in the studies of land use impacts, among which the land use data used is one of the sources of uncertainty. With the development of satellite remote sensing technology, more and more land use data are available (ESACCI-LC 2017; Li et al. 2020), based on which ensemble numerical experiments can be performed and the uncertainties for LUCC impacts might be reduced.

Supplementary Information The online version contains supplementary material available at https://doi.org/10.1007/s00382-023-06959-5.

Acknowledgements This research was funded by National Natural Science Foundation of China under grant no. 41775087, 42141017 and 41875178, National Key R&D Program of China under grant no. 2018YFA0606004, China Postdoctoral Science Foundation (no. 2019M660761), the Program for Special Research Assistant Project of Chinese Academy of Sciences, and Jiangsu Collaborative Innovation Center for Climatic Change.

Authors' contributions D ZHAO designed numerical experiments, performed the analysis and wrote the main manuscript. J ZHA performed analysis on the near-surface wind speed. J Wu participated in the analysis and revision of the manuscript. All authors contributed to the discussions, read and approved the final manuscript.

Data Availability CRU surface air temperature data are available at https://catalogue.ceda.ac.uk/uuid/89e1e34ec3554dc98594a5732622bce9. GPCC precipitation data can be found at https://opendata.dwd.de/climate_environment/GPCC/html/fulldata-monthly_v2020_doi_download.html. NCEP FNL datasets can be downloaded at https://rda.ucar.edu/datasets/ds083.2/. Land use data in the 1980 and 2010 s are available to readers upon request.

Codes availability Computer codes adopted in the data processing and analysis were written in FORTRAN language. All types of figures appear in this manuscript were drawn with Grads (http://cola.gmu.edu/grads/downloads.php) or Origin (https://www.originlab.com/origin). More specific codes in this manuscript are available to readers upon request

Declarations

Ethical approval Not applicable.

Competing interests The authors declare no competing interests.

References

Alkama R, Cescatti A (2016) Biophysical climate impacts of recent changes in global forest cover. Science 351:600–604. https://doi.org/10.1126/science.aac8083

Andrews T, Betts RA, Booth BBB, Jones CD, Jones GS (2017) Effective radiative forcing from historical land use change. Clim Dyn 48:3489–3505. https://doi.org/10.1007/s00382-016-3280-7

Bathiany S, Claussen M, Brovkin V, Raddatz T, Gayler V (2010) Combined biogeophysical and biogeochemical effects of large-scale

forest cover changes in the MPI earth system model. Biogeosciences 7:1383–1399. https://doi.org/10.5194/bg-7-1383-2010

Betts RA (2000) Offset of the potential carbon sink from boreal forestation by decreases in surface albedo. Nature 408:187–190. https://doi.org/10.1038/35041545

Betts RA, Falloon PD, Goldewijk KK, Ramankutty N (2007) Biogeophysical effects of land use on climate: Model simulations of radiative forcing and large-scale temperature change. Agric for Meteorol 142:216–233. https://doi.org/10.1016/j.agrformet.2006.08.021

Boyaj A, Dasari HP, Hoteit I, Ashok K (2020) Increasing heavy rainfall events in south India due to changing land use and land cover. Q J R Meteorol Soc 146:3064–3085. https://doi.org/10.1002/qj.3826

Charney J (1975) Dynamics of deserts and drought in the Sahel. Q J R Meteorol Soc 101:193–202

Chen F, Manning KW, LeMone MA, Trier SB, Alfieri JG, Roberts R, Tewari M, Niyogi D, Horst TW, Oncley SP, Basara JB, Blanken PD (2007) Description and evaluation of the characteristics if the NCAR high-resolution land data assimilation system. J Appl Meteorol Climatol 46:694–713. https://doi.org/10.1175/JAM2463.1

Chinnisamy S, Gassman PW, Secchi S, Srinivasan R (2008) Comparison of Land Use Area Estimates from Three Different Data Sources for the Upper Mississippi River Basin. CARD Technical Report Series 6332, Lowa State University, Center for Agriculture and Rural Development

Defries RS, Field CB, Fung I, Collatz GJ, Bounoua L (1999) Combining satellite data and biogeochemical models to estimate global effects of human-induced land cover change on carbon emissions and primary productivity. Global Biogeochem Cycles 13:803–815. https://doi.org/10.1029/1999GB900037

ESACCI-LC (2017) Land Cover CCI Product User Guide Version 2. Tech Rep. Available at: maps.elie.ucl.ac.be/CCI/viewer/download/ESACCI-LC-Ph2-PUGv2_2.0.pdf

Fita L, Fernandez J, Garcia-Diez M (2010) CLWRF: WRF modifications for regional climate simulation under future scenarios. Proceedings of 11th WRF Users' Workshop, 22–24

Gallo K, Owen T, Easterling D (1999) Temperature trends of the U.S. historical Climatology Network based on satellite designated land use/land cover. J Clim 12:1344–1348. https://doi.org/10.1175/1520-0442(1999)012,1344:TTOTUS.2.0.CO;2

Gao XJ, Xu Y, Zhao ZC, Pal JS, Giorgi F (2006) On the role of Resolution and Topography in the Simulation of East Asia Precipitation. Theor Appl Climatol 86:173–185. https://doi.org/10.1007/s00704-005-0214-4

Gasser T, Crepin L, Quilcaille Y, Houghton RA, Obersteiner M (2020) Historical CO2 emissions from land use and land cover change and their uncertainty. Biogeosciences 17:4075–4101. https://doi.org/10.5194/bg-17-4075-2020

Giorgi F, Coppola E, Solmon F, Mariotti L, Sylla MB, Bi X, Elguindi N, Diro GT, Nair V, Giuliani G, Cozzini S, Güttler Ivan, O'Brien TA, Tawfik AB, Shalaby A, Zakey AS, Steiner AL, Stordal F, Sloan LC, Brankovic C (2012) RegCM4: model description and preliminary tests over multiple CORDEX domains. Clim Res 52:7–29

Harris I, Osborn TJ, Jones P, Lister D (2020) Version 4 of the CRU TS monthly high-resolution gridded multivariate climate dataset. Sci Data 7:109. https://doi.org/10.1038/s41597-020-0453-3

Hirsch AL, Guillod BP, Seneviratne SI, Beyerle U, Boysen LR, Brovkin V, Davin EL, Doelman JC, Kim H, Mitchell DM, Nitta T, Shiogama H, Sparrow S, Stehfest E, van Vuuren DP, Wilson S (2018) Biogeophysical Impacts of Land-Use Change on Climate Extremes in Low-Emission scenarios: results from HAPPI-Land. Earth's Future 6:396–409. https://doi.org/10.1002/2017EF000744

Houghton RA, Nassikas AA (2017) Global and regional fluxes of carbon from land use and land cover change 1850–2015. Global Biogeochem Cycles 31:456–472. https://doi.org/10.1002/2016GB005546

Huang QH, Zhang XC, Liu T (2007) Study on the Precision of land-use data in different spatial scale (in chinese). Geomatics World 5:6. https://doi.org/10.3969/j.issn.1672-1586.2007.02.016

IPCC, The Physical Science Basis. Contribution of Working Group I to the Sixth Assessment Report of the Intergovernmental Panel on Climate Change [Masson-Delmotte V, Zhai P, Pirani A, Connors SL, Péan C, Berger S, Caud N, Chen Y, Goldfarb L, Gomis MI, Huang M, Leitzell K, Lonnoy E, Matthews JBR, Maycock TK, Waterfield T, Yelekçi O, Yu R, Zhou B (eds.)(2021)]. Cambridge University Press, Cambridge, United Kingdom and New York, NY, USA, 2391 pp. https://doi.org/10.1017/9781009157896

IPCC, The Physical Science Basis. Contribution of Working Group I to the Fifth Assessment Report of the Intergovernmental Panel on Climate Change [Stocker TF., Qin D, Plattner G-K, Tignor M, Allen SK, Boschung J, Nauels A, Xia Y, Bex V, Midgley PM (eds.)(2013)]. Cambridge University Press, Cambridge, United Kingdom and New York, NY, USA, 1535 pp. https://doi.org/10.1017/cbo9781107415324.004

IPCC (Climate Change 2007) In: Qin S, Manning D, Chen M, Marquis Z, Averyt M, Tignor KB, Miller M HL (eds) The physical science basis. Contribution of Working Group I to the Fourth Assessment Report of the Intergovernmental Panel on Climate Change [Solomon. Cambridge University Press, Cambridge, United Kingdom and New York, NY, USA, p 996. www.ipcc.ch/report/ar4/wg1

Jehanzaib M, Shah SA, Yoo J, Kim T-W (2020) Investigating the impacts of climate change and human activities on hydrological drought using non-stationary approaches. J Hydrol 588:125052. https://doi.org/10.1016/j.jhydrol.2020

Jia G, Shevliakova E, Artaxo P, De Noblet-Ducoudré N, Houghton R, House J, Kitajima K, Lennard C, Popp A, Sirin A, Sukumar R, Verchot L (2019) Land–climate interactions. In: Climate Change and Land: an IPCC special report on climate change, desertification, land degradation, sustainable land management, food security, and greenhouse gas fluxes in terrestrial ecosystems [Shukla PR, Skea J, Calvo Buendia E, Masson-Delmotte V, Pörtner H-O, Roberts DC, Zhai P, Slade R, Connors S, van Diemen R, Ferrat M, Haughey E, Luz S, Neogi S, Pathak M, Petzold J, Portugal Pereira J, Vyas P, Huntley E, Kissick K, Belkacemi M, Malley J (eds.)]. https://doi.org/10.1017/9781009157988.004

Kalnay E, Cai M (2003) Impact of urbanization and land-use change on climate. Nature 423:528–531. https://doi.org/10.1038/nature01675

Lawrence PJ, Feddema JJ, Bonan GB, Meehl GA, O'Neill BC, Oleson KW, Levis S, Lawrence DM, Kluzek E, Lindsay K, Thornton PE (2012) Simulating the biogeochemical and biogeophysical impacts of transient land cover change and wood harvest in the Community Climate System Model (CCSM4) from 1850 to 2100. J Clim 25:3071–3095. https://doi.org/10.1175/JCLI-D-11-00256.1

Li D, Bou-Zeid E, Barlage M, Chen F, Smith JA (2013) Development and evaluation of a mosaic approach in the WRF-Noah framework. J Geophys Res: Atmos 118:11918–11935

Li HX, Xiao PF, Feng XZ, Yang YK, Wang LX, Zhang WB, Wang XH, Feng WD, Chang X (2017) Using land long term data records to map land cover changes in China over 1981–2010. IEEE J Selected Topics Appl Earth Obs Remote Sens 10:1372–1389. https://doi.org/10.1109/JSTARS.2016.2645203

Li H, Zhang H, Mamtimin A, Fan S, Ju C (2020) A New Land-Use dataset for the Weather Research and forecasting (WRF) model. Atmos 11:350. https://doi.org/10.3390/atmos11040350

Li Y, Li ZL, Wu H, Zhou CH, Liu XY, Leng P, Yang P, Wu WB, Tang RL, Shang G-F, Ma LL (2023) Biophysical impacts of earth greening can substantially mitigate regional land

surface temperature warming. Nat Commun 14:121. https://doi.org/10.1038/s41467-023-35799-4
Liu S, Wang Y, Zhang GJ, Wei LY, Wang B, Yu L (2022) Contrasting influences of biogeophysical and biogeochemical impacts of historical land use on global economic inequality. Nat Commun 13:2479. https://doi.org/10.1038/s41467-022-30145-6
Mueller WA, Jungclaus JH, Mauritsen T, Baehr J, Bittner M, Budich R, Bunzel F, Esch M, Ghosh R, Haak H, Ilyina T, Kleine T, Kornblueh L, Li H, Modali K, Notz D, Pohlmann H, Roeckner E, Stemmler I, Marotzke JA (2018) Higher-resolution version of the Max Planck Institute Earth System Model (MPI-ESM1.2-HR). J Adv Modeling Earth Sys 10:1383–1413
Nisbet EG, Manning MR, Dlugokencky EJ, Fisher RE, Lowry D, Michel SE, Lund Myhre C, Platt SM, Allen G, Bousquet P, Brownlow R, Cain M, France JL, Hermansen O, Hossaini R, Jones AE, Levin I, Manning AC, Myhre G, Pyle JA, Vaughn BH, Warwick NJ, White JWC (2019) Very strong atmospheric methane growth in the four years 2014–2017: implications for the Paris Agreement. Global Biogeochem Cycles 33:318–342. https://doi.org/10.1029/2018GB006009
Niu G-Y, Yang Z-L, Mitchell KE, Chen F, Ek MB, Barlage M, Kumar A, Manning K, Niyogi D, Rosero E, Tewari, Xia YL (2011) The community Noah land surface model with multiparameterization options (Noah-MP): 1. Model description and evaluation with local-scale measurements. J Geophys Res: Atmos 116:D12109. https://doi.org/10.1029/2010JD015139
Oleson KW, Lawrence DM, Bonan GB, Flanner MG, Kluzek E, Lawrence PJ, Levis S, Swenson SC, Thornton PE, Dai AG, Decker M, Dickinson R, Feddema J, Heald CL, Hoffman F, Lamarque J-F, Mahowald N, Niu G-Y, Qian TT, Randerson J, Running S, Sakaguchi K, Slater A, Stöckli R, Wang AH, Yang Z-L, Zeng XD, Zeng XB (2010) Technical description of the version 4.0 of the Community Land Model (CLM). NCAR Technical Note. NCAR/TN–478 + STR
Pongratz J, Reick CH, Raddatz T, Claussen M (2010) Biogeophysical versus biogeochemical climate response to historical anthropogenic land cover change. Geophys Res Lett 37:1–5. https://doi.org/10.1029/2010GL043010
Rasmussen R, Ikeda K, Liu C, Gochis D, Clark M, Dai A, Gutmann E, Dudhia J, Chen F, Barlage M, Yates D, Zhang G (2014) Climate change impacts on the water balance of the Colorado Headwaters: high-resolution regional climate model simulations. J Hydrometeor 15:1091–1116. https://doi.org/10.1175/JHM-D-13-0118.1
Schneider U, Becker A, Finger P, Rustemeier E, Ziese M (2020) GPCC Full Data Monthly Product Version 2020 at 0.5°: Monthly Land-Surface Precipitation from Rain-Gauges built on GTS-based and Historical Data. https://doi.org/10.5676/DWD_GPCC/FD_M_V2020_050
Sherwood SC, Dixit V, Salomez C (2018) The global warming potential of near-surface emitted water vapour. Environ Res Lett 13:104006. https://doi.org/10.1088/1748-9326/aae018
Shi Y, Wang GL, Gao XJ (2017) Role of Resolution in Regional Climate Change Projections over China. Clim Dyn 51:2375–2396. https://doi.org/10.1007/s00382-017-4018-x
Skamarock WC, Klemp JB, Dudhia J, Gill DO, Barker DM, Duda MG, Huang X-Y, Wang W, Powers JG (2008) A description of the Advanced Research WRF Version 3. NCAR Technical Note. NCAR/TN–475 + STR
Vertenstein M, Craig T, Middleton A, Feddema D, Fischer C (2012) CESM1.0.4 user's guide. National Center for Atmospheric Research, Boulder, CO. 2012
Wang SY, Fu CB, Wei HL, QianY, Xiong Z, Feng JM, Zhao DM, Dan L, Han ZW, Su BK, Zhao M, Zhang YC, Tang JP, Liu HN, Wu J, Zeng XM, Chen M, Wang LZ (2015) Regional integrated environmental modeling system: development and application. Clim Change 129:499–510
Ward DS, Mahowald NM, Kloster S (2014) Potential climate forcing of land use and land cover change. Atmos Chem Phys 14:12701–12724. https://doi.org/10.5194/acp-14-12701-2014
Yan ZW, Li Z, Li QX, Jones PD (2010) Effects of site change and urbanization in the Beijing temperature series 1977–2006. Int J Climatol 30:1226–1234. https://doi.org/10.1002/joc.1971
Yang YK, Xiao PF, Feng XZ, Li HX (2017) Accuracy assessment of seven global land cover datasets over China. ISPRS J Photogrammetry and Remote Sens 125:156–173
Zhang W, Villarini G, Vecchi GA, Smith JA (2018) Urbanization exacerbated the rainfall and flooding caused by hurricane Harvey in Houston. Nature 563:384–388. https://doi.org/10.1038/s41586-018-0676-z
Zhao DM (2013) Performance of Regional Integrated Environment modeling System (RIEMS) in precipitation simulations over East Asia. Clim Dyn 40:1767–1787. https://doi.org/10.1007/s00382-012-1660-1
Zhao DM, Wu J (2017a) The influence of urban surface expansion in China on regional climate. J Clim 30:1061–1080. https://doi.org/10.1175/JCLI-D-15-0604.1
Zhao DM, Wu J (2017b) The impact of land use and land cover changes on east asian summer monsoon precipitation using the WRF-mosaic approach. Atmos Sci Lett 18:450–457. https://doi.org/10.1002/asl.788
Zhao DM, Wu J (2017c) Inclusion of land use changes in long-term regional climate simulations over East Asia. Atmos Sci Lett 18:187–192. https://doi.org/10.1002/asl.744
Zhou RB, Lin MZ, Gong JZ, Wu Z (2019) Spatiotemporal heterogeneity and influencing mechanism of ecosystem services in the Pearl River Delta from the perspective of LUCC. J Geogr Sci 29:831–845. https://doi.org/10.1007/s11442-019-1631-0